Multimodal imaging and stochastic percolation simulation for improved quantification of effective porosity and surface area in vesicular basalt

Christopher Zahasky[a,*], Dana Thomas[b,c], Juerg Matter[d,e], Kate Maher[f], Sally M. Benson[a]

[a] *Department of Energy Resources Engineering, Stanford University, Stanford, CA*
[b] *Department of Geological Sciences, Stanford University, Stanford, CA*
[c] *now at the Jackson School of Geosciences, University of Texas at Austin, Austin, TX*
[d] *Department of Ocean and Earth Science, University of Southampton, Southampton, UK*
[e] *Lamont-Doherty Earth Observatory, Columbia University, Palisades, NY*
[f] *Department of Earth System Science, Stanford University, Stanford, CA*

Abstract

Improved methods for predicting fluid transport and vesicle connectivity in heterogeneous basalts are critical for determining the long-term reaction and trapping behavior of sequestered carbon dioxide and maximizing the efficiency of geothermal energy production. In this study we measured vesicle geometry, pore connectivity, and vesicle surface area of three basalt cores from the CarbFix carbon storage project in Iceland using a combination of micro-computed tomography, clinical computed tomography, and micro-positron emission tomography. A vesicle percolation simulator was then constructed to quantify vesicle connectivity across a complete range of porosities, pore size distributions, and microporosity conditions. Percolation simulations that incorporate important geologic features such as microporosity are able to describe the trend of experimental measurements made in this study and in previous work, without relying on statistical or empirical techniques. Simulation results highlight and quantify the trade-off between storage capacity and reactive surface area in high porosity basalts. Experiment and simulation results also indicate that there is very limited connected pore space below total porosity values of 15%, guiding improved site selection for large scale CO_2 storage projects. Use of this stochastic percolation simulation method for basalt storage reservoir evaluation will enable more accurate storage capacity and mineral trapping estimates.

Keywords: carbon capture and storage; geothermal energy; positron emission tomography; effective porosity; micro-CT; percolation simulation

*Corresponding author: zahasky@stanford.edu

Graphical abstract

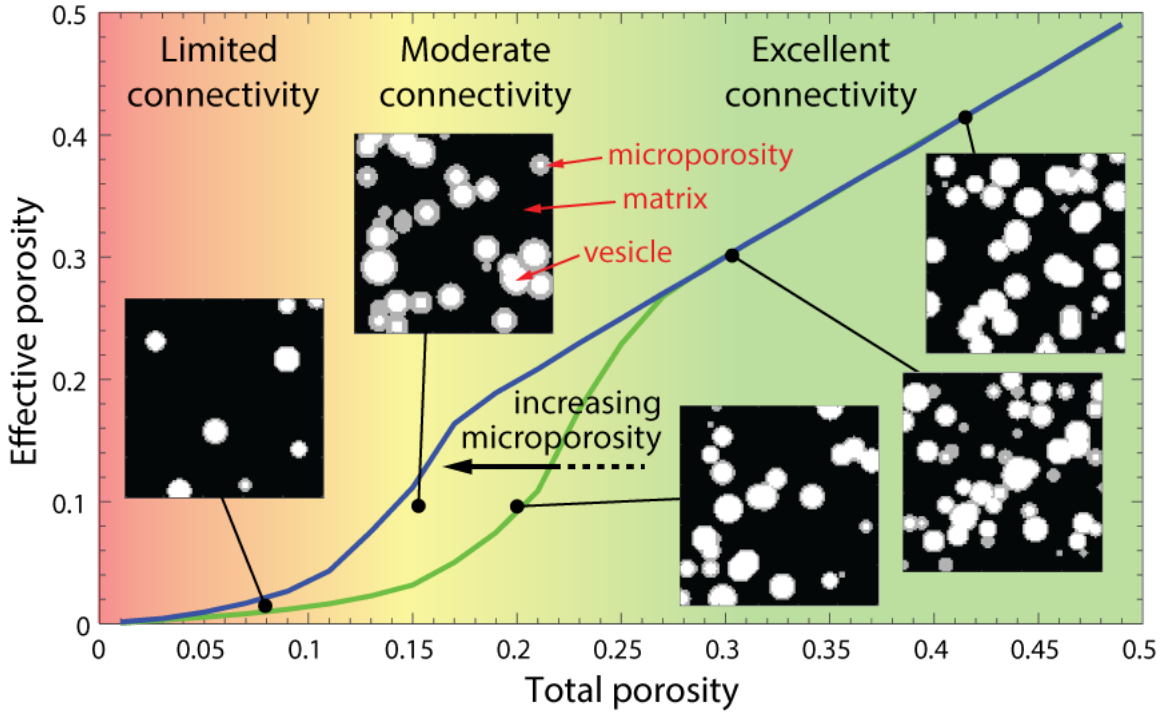

1. Introduction

Wide scale implementation of carbon capture and storage (CCS) and geothermal energy production has the potential to significantly reduce anthropogenic carbon dioxide emissions relative to current fossil fuel-based power generation facilities and production operations (Socolow and Pacala, 2004; Szulczewski et al., 2012; Benson and Cook, 2005). Due to the global scale and geographic extent of CO_2 emissions, a number of different types of carbon storage reservoirs are needed. Storage reservoirs include deep saline aquifers (Michael et al., 2010), abandoned oil and gas fields (Benson and Cook, 2005), and basalt or ultramafic rock reservoirs (Goldberg et al., 2010; Gislason and Oelkers, 2014). While saline aquifers and abandoned oil and gas fields have been studied and characterized extensively for CO_2 carbon storage, much remains to be learned about the storage potential, injection viability, and large-scale CO_2 trapping potential in basalt reservoirs.

Basalt formations are enticing reservoirs for long-term CO_2 storage due to their potential to immobilize large volumes of CO_2 through mineral trapping (Gislason and Oelkers, 2014), and their geographic extent in areas lacking saline aquifers or abandoned oil and gas reservoirs. Basalts are particularly favorable to mineral storage of CO_2 due to the presence of highly reactive silicate minerals and glasses rich in divalent cations that are necessary to promote formation of stable carbonate minerals. Basaltic provinces with potential for storing large volumes of CO_2 include the Columbia River flood basalts in the Pacific Northwest US (McGrail et al., 2006, 2017; Tollefson, 2013), the Central Atlantic Magmatic Province basalts on the east coast of the US (Goldberg et al., 2010), basaltic oceanic crust and volcanic islands such as the Hawaiian Islands and Iceland (Goldberg et al., 2008; Matter et al., 2016; Snæbjörnsdóttir et al., 2014; Snæbjörnsdóttir and Gislason, 2016; Snæbjörnsdóttir et al., 2018; Aradóttir et al., 2012; Rezvani Khalilabad et al., 2008), and the Deccan flood basalts spread across west-central India (McGrail et al., 2006; Holloway et al., 2009; Shrivastava et al., 2016).

Accurate prediction of large-scale heat transfer in geothermal systems, and fluid transport and CO_2 trapping in CCS storage reservoirs, requires measurements of basalt reactivity, vesicle-matrix surface area, pore space geometry, and porosity (Snæbjörnsdóttir et al., 2018; Callow et al., 2018; Aradóttir et al., 2012; Wolff-Boenisch and Galeczka, 2018). A wide range of methods exist to characterize the total porosity, effective porosity, permeability, and estimate surface area of basaltic samples. These methods include point counting (Sigurosson et al., 2000; Franzson et al., 2008; Saar and Manga, 1999; Manning and Bird, 1991), helium porosimetry/gas expansion techniques (Saar, 1998; Sigurosson et al., 2000; Lamur et al., 2017; Mueller et al., 2005; Ellis and Wright, 2006; Heap et al., 2014; Farquharson et al., 2015; Kushnir et al., 2016), and the Brunauer Emmet Taylor (BET) surface area measurement method (Navarre-Sitchler et al., 2013; Beckingham et al., 2016; Kumar et al., 2017; Landrot et al., 2012; Kushnir et al., 2016), respectively. With the advancements in imaging methods, total porosity, pore geometry, and surface area can also be measured with micro X-ray computed tomography (micro-CT) (Callow et al., 2018; Song et al., 2001; Navarre-Sitchler et al., 2009; Beckingham et al., 2017; Luhmann et al., 2017; Bai et al., 2010; Shin et al., 2005; Polacci et al., 2008, 2012), neutron scattering (Navarre-Sitchler et al., 2013; Luhmann et al., 2017), and scanning electron microscopes (SEM) (Beckingham et al., 2016; Landrot et al., 2012).

Despite these advancements, measurements of effective porosity–also referred to as connected porosity–and effective surface area are typically performed on very small samples (< 1 cm^3) at ambient conditions and without the benefit of directly observing fluid transport in the sample. Clinical positron emission tomography (PET) and, more recently, small-bore preclinical micro-PET has been used to image flow pathways and quantify solute advection and diffusion at the continuum scale under elevated pressure and temperature conditions (Boutchko et al., 2012; Kulenkampff et al., 2015; Fernø et al., 2015; Pini et al., 2016; Hu et al., 2017; Brattekas et al., 2016; Goethals et al., 2009; Lippmann-Pipke et al., 2017; Zahasky and Benson, 2018). When combined with other imaging modalities such as micro-CT and clinical CT, micro-PET imaging is capable of characterizing complex fluid transport behavior and sample properties of geologic materials.

The complexity and laborious nature of many experimental measurements of total porosity, effective porosity, total surface area, and effective surface area limit the number of samples that may be characterized. Experimental limitations make it challenging to understand basalt vesicle connectivity and surface area trends that can vary due to emplacement thermodynamic conditions, interactions with water, and degassing activity—along with potential hydrothermal alteration, metamorphism, stress history, and weathering (McGrail et al., 2006; Song et al., 2001). The development of numerical models that can incorporate experimental measurements of these geologic characteristics and predict vesicle connectivity and surface area are essential for reactive transport simulation modeling, predicting geothermal reservoir heat transfer efficiency, and robustly quantifying basalt reservoir CO_2 storage capacity.

In this study, pore connectivity, advective pathways, and surface area were characterized in vesicular basalt cores to better understand CO_2 storage and trapping properties relevant in CCS projects. Three cores were obtained from the CarbFix CO_2 storage pilot project, two low porosity ($<$10%) cores, and one higher porosity ($\sim$30%) core. Using a combination of micro-CT, clinical CT, and micro-PET imaging during tracer injection coreflooding experiments, it was possible to measure effective and total porosity, and effective and total vesicle surface area. Sample analysis and imaging results also highlight the importance of rims of microcracks and microporous features

on vesicle connectivity. Motivated by these observations, a vesicle percolation simulator was constructed in order to generalize vesicle connectivity across a complete range of porosities, pore size distributions, and microporosity conditions. Vesicular basalts are the focus of this study as they have been proposed as the principle basalt feature associated with high CO_2 injectivity and storage volume (McGrail et al., 2006). Experimental characterization from this study and other reports in literature are compared with the simulation results. The findings of this study highlight the trade-off between pore volume and surface area in high porosity basalts and provide a method for better predicting effective porosity based on experimental observations of vesicle properties.

2. Materials and Methods

The focus of the CarbFix project, managed by the geothermal power company Reykjavík Energy, is to validate the feasibility of injecting CO_2 dissolved in water into subsurface mafic reservoirs for long-term storage. From January to March 2012 and June to August 2012, 175 tons of CO_2 gas and 73 tons of a CO_2-H_2S gas mixture from the Hellisheidi geothermal power plant were dissolved in water and injected into a subsurface basaltic formation (Matter et al., 2016). Cores used in this study (KB2017a, KB2017b, KB2017c) were obtained from well KB01, drilled in 2014 between the injection well, HN-02, and the monitoring well, HN-04. All of the cores were 4.5 cm in diameter and between 3.5 and 10.1 cm in length. A complete summary of sample dimensions and well depth locations is included in the Table 1. An important characteristic of sample KB2017b was that it contained a natural axial fracture that ran the entire length of the core. Samples KB2017a and KB2017c did not contain visible fractures.

The porosity analysis of the each of the samples was performed on multiple small plugs cored adjacent to each of the samples. Effective porosity measurements were performed with a Micromeritics AccuPyc II Helium Pycnometer with a 3.5 cm^3 volume chamber. The mean Helium porosity measurement for each sample is included in Table 2 with measurement details in the Excel sheet provided in the Supplementary Material.

The mineralogy and composition of the Carbfix cores have been analyzed in previous studies by a number of methods including optical petrography and electron microscopy (Alfredsson et al., 2013; Snæbjörnsdóttir et al., 2018; Thomas, 2018). An important observation from the optical petrography and backscatter electron images of the samples, presented in detail in Thomas (2018), is the rim of microcracks and other microporous features surrounding many of the vesicles as highlighted in Figure 1. These features are below the resolution of micro-CT imaging. Similar microcracks and microporous features have been observed in other experimental studies of vesicular basalts (Lamur et al., 2017; Mueller et al., 2005; Navarre-Sitchler et al., 2009, 2013; Luhmann et al., 2017).

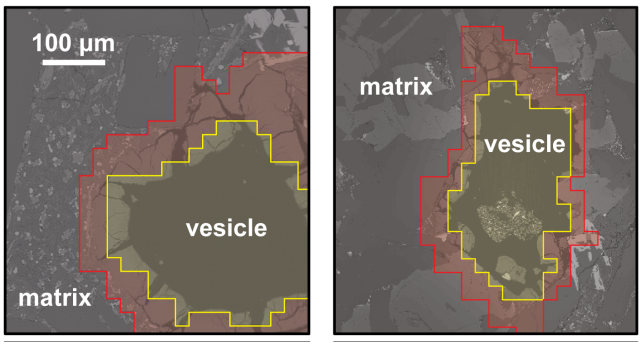

Figure 1: Two backscatter electron images of vesicles in basalt sample directly adjacent to KB2017a and KB2017c. Yellow areas highlight the pore space likely identified by micro-CT imaging for porosity calculations. The red region indicates the microporous rim around the vesicle, which has limited porosity but provides vesicle connectivity.

2.1. Coreflooding Experiments

To measure the total and effective porosity and total and connected surface area in the three CarbFix cores, a multiscale and multimodal characterization process was employed. Prior to coreflooding, the cores were scanned using a Zeiss 3D X-ray microscope to obtain micro-CT images of the pore structure. The operating conditions for the micro-CT were 140 kV and 10 W using a 0.4x objective, with a two second exposure time. The reconstructed micro-CT images of all of the samples had voxel side lengths of approximately 50 μm (exact dimensions of each scan can be found in the Excel sheet in the Supplementary Material).

Following initial characterization and micro-CT imaging, coreflooding experiments were performed to measure permeability and image pore space connectivity with micro-PET. To enable injection, quantification, and disposal of radioactive tracers for micro-PET imaging, a standard core flooding apparatus (Perrin and Benson, 2010) was adapted as described in detail in Zahasky and Benson (2018). A PET scan was not performed on core KB2017c because it had a permeability less than 1 μD and therefore steady-state injection conditions could not be reached.

The process for loading the cores into the custom aluminum coreholder was to first wrap the core with Teflon tape, then two layers of heat shrinkable wrap, and finally a Viton sleeve. The Teflon tape wrap is essential to prevent fluid bypass in low permeability cores, as any fluid bypass is obvious in the PET images. The cores were then loaded into an aluminum core holder and water was injected into the volume between the outside of the Viton sleeve and the internal wall of the core holder to provide confining pressure on the rock. Confining pressure was chosen to provide and maintain an effective pressure (i.e. confining/overburden pressure minus pore pressure) of ~2-3.1 MPa at all times. The cores were saturated with MilliQ water by injecting at constant flow rate for a minimum of twelve hours. Fully saturating the samples with water

Table 1: Basalt samples summary

Sample	Length (cm)	Diameter (cm)	Permeability (mD)	Well depth (mbs)
KB2017a	3.5	4.5	0.004	400.1
KB2017b	10.1	4.5	500	440.1
KB2017c	4	4.5	<0.001	400.0

is important for preventing multiphase flow during radiotracer injection and micro-PET imaging.

Once the cores were loaded in the coreholder and saturated with water, each core was scanned using a clinical General Electric Hi-Speed CT scanner. The scanner voltage and current settings were 120 kV and 200 mA, respectively. The reconstructed images had a voxel size of 0.3125 mm x 0.3125 mm x 1.25 mm. The clinical CT scan was used to assist with the registration of the micro-CT images with the micro-PET images because the clinical CT has high enough resolution to uniquely identify large individual vesicles from the micro-CT scan, and the clinical CT can image the exact orientation of the core in coreholder for registration with the micro-PET scan.

For the micro-PET scans on samples KB2017a and KB2017b, the Fludeoxyglucose ($[^{18}F]$FDG) radiotracer was diluted into an ISCO pump initially containing MilliQ water. Fludeoxyglucose is a widely available, conservative tracer—as confirmed by radioactivity mass balance from tracer curve analysis—and has a half-life of 109.7 minutes. These characteristics make FDG an ideal choice for multihour tracer injection studies. Once mixed, the solution in the tracer pump was injected through the core (KB2017a: 0.014 mL/min; KB2017b: 0.2 mL/min). A minimum of one pore volume of fluid was injected into each sample in order to highlight the connected pores. Due to the difference in pore volume, only 5 mL of radiotracer was injected in sample KB2017a while 30 mL of tracer was injected into KB2017b. The micro-PET scans were performed using a Siemens pre-clinical Inveon DPET scanner at the Stanford Center for Innovation in In-Vivo Imaging. The PET scans were reconstructed with 3D Ordered Subset Expectation Maximization using Maximum A Priori (OSEM-OPMAP)(Hudson and Larkin, 1994). Reconstructed images had square voxels with a side length of 0.8 mm for all scans.

2.2. Imaging Analysis

Following image acquisition and reconstruction, the micro-CT and micro-PET scans were manually registered with the clinical CT scans using Avizo (Scientific, 2018). The micro-CT was segmented in Avizo to determine the location and geometry of the vesicles and matrix. While countless methods exist for porosity segmentation (Iassonov et al., 2009), we chose to segment the micro-CT images with the watershed method due to its relative ease and robustness (Vincent and Soille, 1991). Examples of this segmentation for KB2017a and KB2017b are illustrated in Figure 2 along with the calculated vesicle size distributions for all three samples. All of the samples show a log-normal distribution of pore radii as has commonly been observed in previous studies (Callow et al., 2018; Shin et al., 2005; McGrail et al., 2006; Song et al., 2001). It is important to note that the presence of any fractures in KB2017a and some regions of the axial fracture in KB2017b are below the resolution of the micro-CT and clinical CT scans.

Once registered, micro-PET data and segmented micro-CT data were exported to Matlab. The pore space identified from the micro-CT images was used to calculate the total porosity and total surface area. The effective porosity, and effective surface area, was determined by identifying the vesicles from the micro-CT scan that overlapped with the location of radiotracer from the registered PET data (for example see left images in Figure 2). Matrix material identified in the segmented micro-CT scans may contain radiotracer due to (1) micro-PET spatial resolution limitations, (2) radiotracer present in features below the micro-CT resolution (i.e. features connecting vesicles in KB2017a), or (3) slight offsets in the micro-CT and micro-PET plane of view as a result of different voxel sizes. Due to the minimal amount of radioactivity injected for the PET scans, if any part of a vesicle (as defined from the registered micro-CT scan) contained radiotracer, the entire vesicle—and all additional overlapping vesicles—was considered connected and therefore included in the effective porosity calculations. The numerical methods for calculating the porosity and surface area were the same as those used in the following section to calculate porosity and surface area in the simulation models. Using the same algorithms for pore structure characterization in both the imaging and numerical models provided consistency between the simulation and experimental analysis.

2.3. Stochastic Percolation Simulation

To generalize the experimental observations of connectivity, porosity, and surface area across a range of basalt porosity, microporosity in the form of microcracked vesicle rims, and vesicle size distribution conditions, a percolation simulator was developed to generate stochastic models of vesicle distribution. Percolation theory is a statistical method for describing systems that exhibit approximately random behavior (Sahimi, 1994; Ellis and Wright, 2006; Blower, 2001; Walsh and Saar, 2008; Bai et al., 2010). By calculating the connectivity, porosity, and surface area of the vesicles in each percolation model, it is possible to correlate effective porosity and surface area with total porosity.

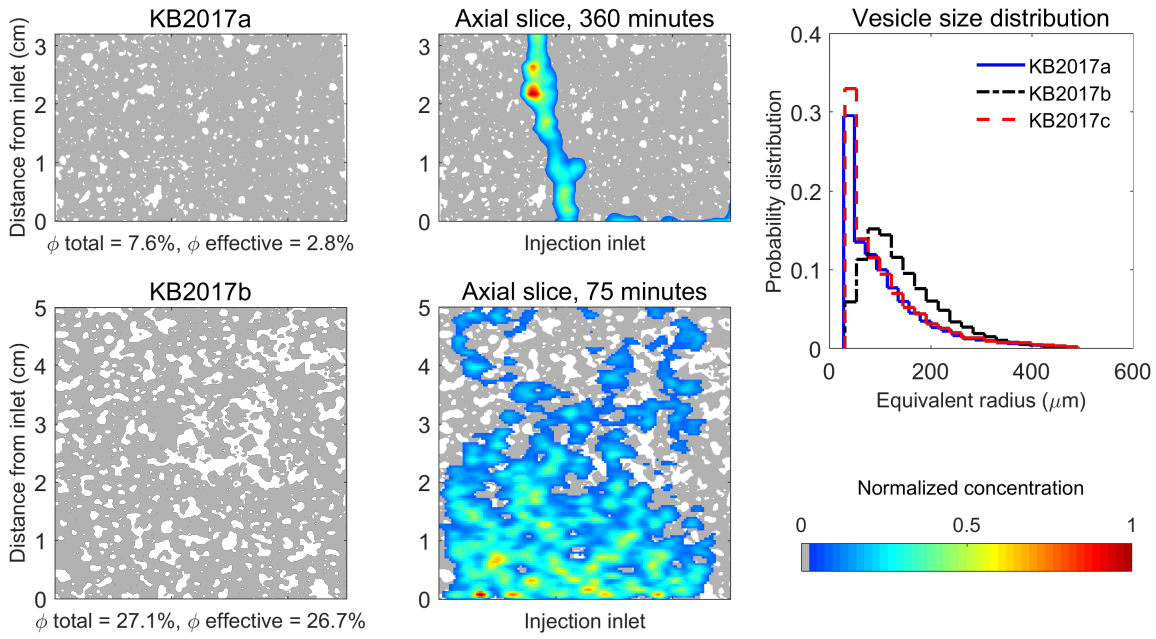

Figure 2: (Upper left) Segmentation results of a center slice of sample KB2017a. (upper middle) Example micro-PET scan results for sample KB2017a after 6 hours, and approximately 3 PV, of radiotracer injection. (Lower left) Segmentation results of center slice of inlet half of sample KB2017b. (lower middle) Example micro-PET scan results for sample KB2017b after 75 minutes, and approximately 0.5 PV, of radiotracer injection. The colorbar indicates normalized radiotracer concentration. (upper right) Vesicle size distribution plot from micro-CT analysis of all three samples. Vesicle equivalent radius is calculated by summing the total number of voxels in each vesicle and calculating the radius if the vesicles were spherical.

The percolation simulator was written in Matlab and propagates one 3D spherical vesicle during each iteration (n) and randomly places the vesicle in a synthetic 3D model. Figure 3 illustrates the center slice of an example simulation at different iterations. During each iteration, the radius of the propagated vesicle is determined by selecting a random value from a radii distribution array that is constructed based on a probability distribution function such as those observed experimentally (right plot in Figure 2). To reduce computation memory requirements the vesicle locations are recorded in an $m \times 4$ array. The columns of this array contain the x, y, and z grid cell coordinates and vesicle identification number; m is the total number of grid cells in which there is pore space in the synthetic 3D basalt model. If a new vesicle is propagated on a grid cell where a vesicle is already present then the vesicles are determined to be connected and are assigned the same vesicle identification number. The vesicle identification number is used to efficiently determine the extent of connectivity between vesicles in the 3D model. After some incremental change in porosity (usually 0.1%) the following model properties are calculated:

Total porosity (ϕ_T), defined as the total number of grid cells containing the vesicles (m) divided by the total number of grid cells in the model (g).

$$\phi_T = \frac{m}{g} \tag{1}$$

Effective porosity (ϕ_E), defined as the number of grid cells continuously connected to left side of model (m_c) divided by the total number of grid cells in the model. In a physical model this would be the porosity accessible by fractures spaced at 2x the synthetic model width. The evolution of effective porosity versus total porosity in 50 simulations is indicated by the red lines in the top of Figure 4.

$$\phi_E = \frac{m_c}{g} \tag{2}$$

Percolation threshold porosity, defined as the porosity at which a volume of vesicles is continuously connected to the left and right side of the model. Above the percolation threshold porosity there is a path that fluid can follow through interconnected vesicles from the left side to the right side of model. This is often termed the percolation threshold in percolation theory literature (Sahimi, 1994). In a system with no fractures this would be the threshold above which it is possible to maintain large scale injection through advective fluid transport. The percolation threshold porosity in 50 simulations is illustrated by the vertical black lines in the top of Figure 4.

Total volume-normalized surface area ($\tilde{s_T}$) of all of the vesicles in the model (blue lines on the bottom plot in Figure 4). Total volume-normalized surface area is calculated by counting the number of grid cell faces that lie at the interface between all vesicles and matrix (f_T) divided by the total number of grid cells

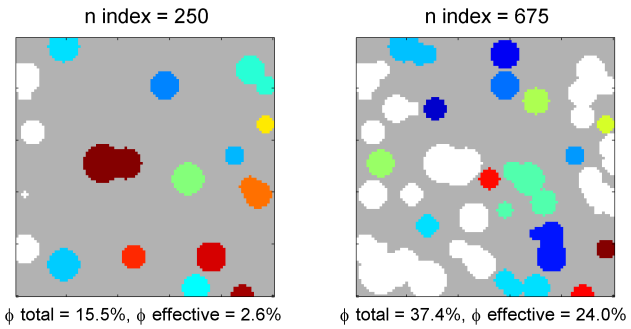

Figure 3: Center slice of 3D simulation model at increasing iterations as labeled by the n value in title. White vesicles are those that are connected—though not necessarily in the plane of view—to the left side of the model. Grey area is impermeable rock matrix. Vesicles of other colors are isolated clusters. For comparison with experimental images, model slices would have a side length equivalent to approximately 3 mm. However, porosity values are independent of model size.

in the model (Shin et al., 2005).

$$\tilde{s_T} = \frac{f_T}{g} \tag{3}$$

Volume-normalized effective surface area ($\tilde{s_E}$) of all vesicles contributing to effective porosity (red lines in the bottom plot in Figure 4). Effective volume-normalized surface area is calculated by counting the number of grid cell faces that lie at the interface between effective porosity vesicles and the matrix (f_E), divided by the total number of grid cells in the model.

$$\tilde{s_E} = \frac{f_E}{g} \tag{4}$$

A simulation terminates when a specified total porosity threshold is reached (e.g. 60%). The assumptions of this percolation simulator are that there is no flow through matrix, individual vesicles are spherical (although clusters of individual spheres form non-ideal shapes), the vesicle geographical distribution is random (e.g. no interaction from mineral crystallization), and vesicle surfaces are planar due to cubic structure of the simulation grid. It has been suggested that specific surface area calculations by direct counting of voxel faces may overestimate surface area due to the ′staircasing′ effect (Song et al., 2001). However, surface area calculations could also be underestimated by ignoring any vesicle surface roughness behavior that has been observed in basalt samples (Navarre-Sitchler et al., 2013; Luhmann et al., 2017). Detailed vesicle surface characterization (such as the BSE images in Figure 1) can be used to determine whether surface smoothing or incorporation of a surface roughness factor is necessary for a given geologic sample (Beckingham et al., 2016; Wells et al., 2017).

All models described in this and the following section have a side length of 120 grid cells ($g = 120^3$) and a normal vesicle radius distribution with a mean radius of five

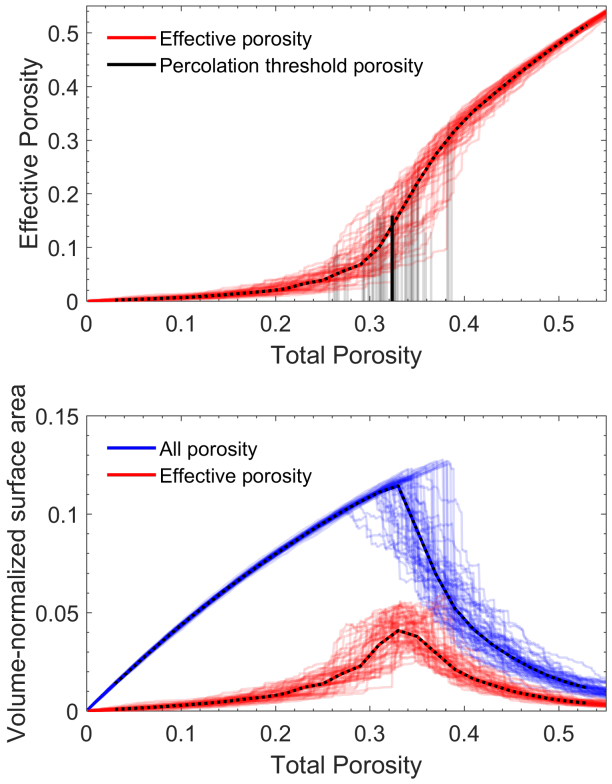

Figure 4: (top) Plot of calculated effective porosity (red lines) and percolation threshold porosity (black lines) following the completion of 50 simulations without including microporosity. (bottom) Plot of volume-normalized surface area of all porosity (blue lines) and effective porosity (red lines). Connected surface area (not shown) is zero until percolation threshold and then follows the effective porosity line. Dashed black lines in both plots represent median trends of the 50 simulations. All models have a normal vesicle radius distribution with a mean radius of five grid cells.

grid cells. Sensitivity analysis described in Appendix A indicates that the median trend of the percolation simulations does not vary with system size (i.e. total number of grid cells) or vesicle radii distribution indicating that detailed knowledge of vesicle topology and size distributions may not be necessary to estimate vesicle connectivity. This agrees with percolation theory predictions that as system size approaches infinity, a single percolation threshold value is reached (Sahimi, 1994). Physical length scales are purposely neglected in the models to highlight scale-independence of the median connectivity behavior. The median percolation threshold in the top of Figure 4 (bold black vertical line) is approximately 0.32, a value nearly equal to the percolation threshold of 0.3116 predicted for a 3D simple cubic sphere system (Sahimi, 1994). These comparisons with analytical predictions serve to validate the accuracy of the numerical model.

The results in the lower plot in Figure 4 highlight that the effective surface area is significantly lower that the total surface area and that the relationship between surface area and total porosity is nonmonotonic. As porosity of the model increases above the percolation threshold, both the total and effective surface area begin to decrease due to higher vesicle overlap and connectivity. This behavior is not captured in analytical expressions of surface area as a function of porosity (McGrail et al., 2006) and highlights an important benefit of percolation simulation analysis.

2.4. Simulations Accounting for Microporosity

Petrographic thin section analysis and backscatter electron imaging from the experimental work (Figure 1), and observations in previous studies, highlight the importance of accounting for rims of microcracks and microporosity around the vesicles in order to properly generalize vesicle connectivity. To account for microporous material in the percolation simulations, a rim of microporous material was added to the outside of the vesicles percolated in the synthetic model. In the simulations, if the microporous region overlapped between different vesicles then they were considered connected for the effective porosity calculations (see Figure 5 for illustration). For the simulations in this study, the microporous region was assumed to have no impact on total porosity or surface area. However, this feature could easily be assigned a secondary porosity value similar to dual-porosity features commonly incorporated into transport simulation models (Gerke and van Genuchten, 1993).

Variation in microporous rim width was examined by running 50 simulations with each model having 1 and 2 grid cell widths of microporosity around every vesicle. The effective versus total porosity results of these simulations can be seen in the Figure 6. The median trend of simulations with 1 and 2 grid cell widths of microporosity are shown in Figure 7. The role of larger thoroughgoing fractures on vesicle connectivity and system conductivity are beyond the scope of this study.

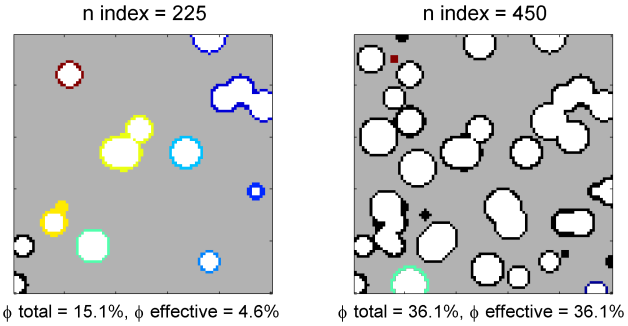

Figure 5: Center slice of 3D simulation model accounting for microporosity—with a one grid cell width microporosity rim–at two different iteration times (n value in title). The white portion of vesicles is volume included in total porosity calculations, colored or black rim material is included in the determination of vesicle connectivity is not included in porosity calculations. Black rimmed vesicles are those that are connected to the left side of the model. Vesicles rimmed with different colors are isolated clusters.

3. Results

3.1. Experimental Results

The experimental measurements of effective porosity versus total porosity are summarized in Figure 7 along with data from several studies utilizing alternative imaging methods such as neutron scattering (Navarre-Sitchler et al., 2013), micro-CT (Callow et al., 2018), and synchrotron micro-CT (Song et al., 2001) for characterizing effective and total porosity of different basalts. Specifically, the samples analyzed in Navarre-Sitchler et al. (2013) were composed of basalt porphery with plagioclase phenocrysts and the samples in Song et al. (2001) were vesiculated, calcite-filled vesiculated, and scoria tephra basalts. Analysis in Callow et al. (2018) was also performed on Carbfix basalt samples that had olivine tholeitte composition. A summary of sample porosity and surface area measurements from the imaging registration, segmentation, and analysis is provided in Table 2.

In sample KB2017a, the PET tracer experiment revealed a discrete, highly localized region of flow after 6 hours of radiotracer injection as illustrated by a center slice of the segmented micro-CT and micro-PET in Figure 2. This likely results from sub-resolution microcracks and highlights the fact that most of the vesicles within the sample were disconnected. This highly localized flow behavior leads to an effective porosity (2.8%) that is significantly lower than the total porosity (7.6%). Sample KB2017c was found to have a porosity of 6.4%, and the effective porosity was determined to be zero due to the very low permeability ($< 1\mu$D), which prevented fluid transmission with the coreflooding system. This is consistent with other experimental and imaging work that indicates limited connectivity and very low permeability of unfractured samples with porosity values less than 10% (Bai et al., 2010; Mueller et al., 2005).

As expected from the extent radiotracer distribution in Figure 2, most of the vesicles in sample KB2017b were

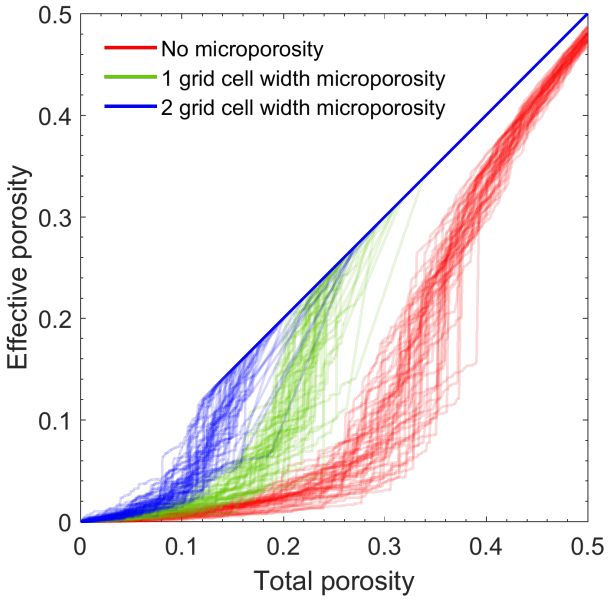

Figure 6: Effective porosity versus total porosity for 150 total simulations with different microporous rim widths. The red lines are simulations with no microporosity, green lines are simulations with microporous rim widths equal to one simulation grid cell, the blue lines are simulations with microporous rims equal to two grid cells.

interconnected (total porosity: 27.1%, effective porosity: 26.7%). Near the inlet of the core nearly all of the pores were filled with radiotracer, however as some of the interconnected vesicle pathways terminated there were several regions near the outlet of the core that had minimal or no radiotracer after more than one pore volume of radiotracer injection.

Experimental measurements from this study agree well with the observations from previous studies by Navarre-Sitchler et al. (2013); Song et al. (2001); Callow et al. (2018), which found very little connected porosity in samples with less than 15% porosity. Between 10% and 25% porosity there is a wide range of trends between effective and total porosity, and above 25% porosity effective porosity and total porosity are nearly equal. Several studies have observed this general relationship between effective porosity and total porosity and described this relationship with empirical percolation (Navarre-Sitchler et al., 2009; Blower, 2001), analytical (McGrail et al., 2006), or linear (Saar and Manga, 1999) functions.

3.2. Stochastic Percolation Simulation Results

The simulation results summarized in Figure 6 and 7 demonstrate that as the thickness of the microporous rim increases the vesicles become more interconnected and therefore the effective porosity at a given total porosity increases. With the addition of microporosity, the simulation results are consistent with the experiments conducted here and with previously reported data (Figure 7).

Table 2: Summary of experimental results. Additional details are provided in Excel file in Supplementary Material.

Sample	Total porosity (%)[a]	Effective porosity (%)[b]	Mean helium porosity (%)	Normalized total surface area (1/vox)	Normalized effective surface area (1/vox)
KB2017a	7.6	2.8	12.5	0.033	0.0113
KB2017b	27.1	26.7	33.9	0.053	0.05
KB2017c	6.4	0	12.1	0.027	0

[a] From micro-CT; [b] From micro-CT and micro-PET;

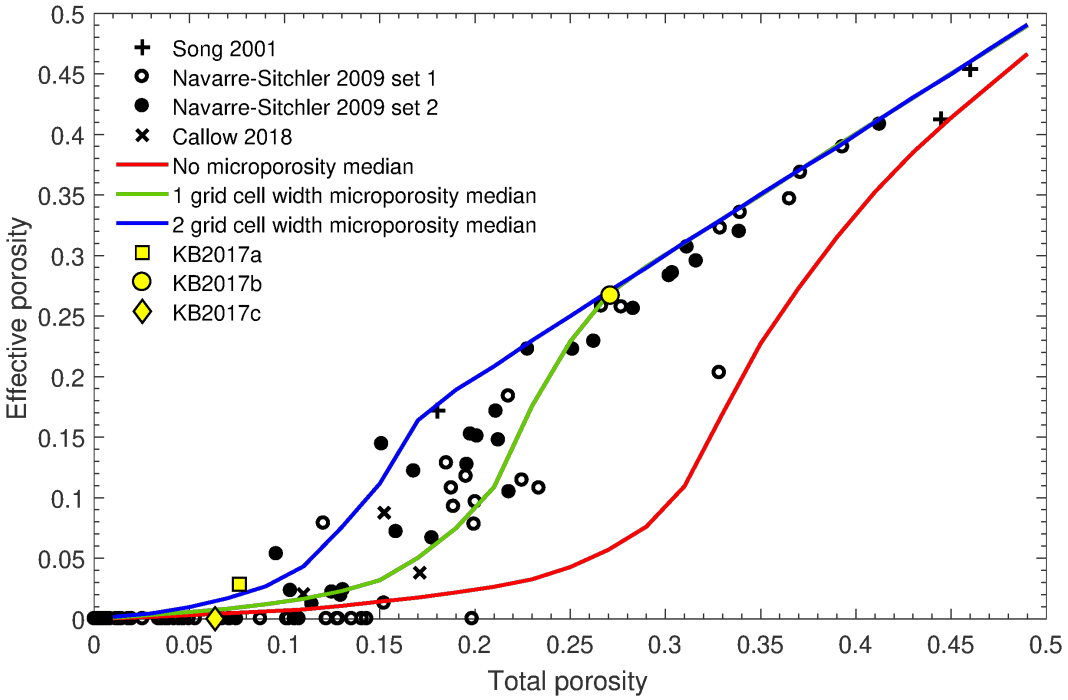

Figure 7: Experimentally measured effective porosity and total porosity from this study (yellow symbols) and other published studies (black symbols). The Navarre-Sitchler data sets used 4.4 μm × 4.4 μm × 4.4 μm resolution images with porosity calculated in sub-sampled cubes with side lengths of 110 μm (set 1) and 220 μm (set 2). Solid lines are the median trends of 50 percolation simulations with no microporosity (red line), 1 grid cell width of microporosity (green line), and 2 grid cell widths of microporosity (blue line).

4. Discussion

The stochastic percolation simulation model results agree well with experimental data from this and previous studies by Navarre-Sitchler et al. (2013); Song et al. (2001); Callow et al. (2018) when microfractured vesicle rims and microporosity are taken into account. The porosity of the modeled vesicular basalts increases as percolated vesicle density and total vesicle volume increases. At low porosity values there is very limited connectivity in the system making fluid transmission difficult. Between a total porosity of 10-25% vesicle connectivity increase rapidly and as basalt porosity increases above 25% porosity most of the vesicles become interconnected. Above a total porosity of around 30% surface area also is shown to begin to decrease. These trends in connectivity agree well with previous experimental and modeling studies analyzing permeability as a function of basalt porosity (Mueller et al., 2005; Costa, 2006; Farquharson et al., 2015; Kushnir et al., 2016). Use of the percolation simulation models to specifically estimate permeability as function of total porosity is an area for future work.

Using a combination of micro-CT, clinical CT, and micro-PET it is possible to measure total porosity, total surface area, effective porosity, and effective surface area. The advantage of this method over previous experimental methods is that measurements directly observe fluid flow in the core, at elevated pressures and temperatures, as a basis for calculating effective porosity and surface area. Direct imaging of pore size and geometry provides more accurate vesicle size distributions than using the cylindrical pore model, or other simplified models, to infer pore sized distribution from mercury injection capillary pressure analysis. In addition, larger intact samples are analyzed, thus reducing edge effects which tend to overestimate effective porosity for small samples. Previous studies utilizing the method of gas expansion pycnometry for determining connectivity in basalts found very little difference between effective porosity and total porosity except at very low (<10%) total porosity values (Saar and Manga, 1999; Sigurosson et al., 2000). While the experimental imaging data from this study and those by Song et al. (2001) and Navarre-Sitchler et al. (2009), as well as nonimaging-based measurements described in Colombier et al. (2017), support the observation of very limited effective porosity below a total porosity of 10%. Experimental imaging measurements indicate that in some systems effective porosity may not approach total porosity until values approach or exceed 25%. Differences in effective porosity measurements between studies are likely the result of variability in basalt formation and weathering, sample preparation, potential edge effects in small samples (Norton and Knapp, 1977), and fluids (e.g. helium versus water) used to measure porosity (Washburn and Bunting, 1922).

Experimental data of effective porosity versus total porosity indicate several trends that vary as function of total porosity. The scattering of data around these trends arise from complex variations associated with basalt formation, weathering, secondary mineral formation, and mechanical deformation. These features may result from vesicle shape variation, nonrandom vesicle distribution, and variability in sample microporosity and fracture extent. Percolation simulations illustrate the ability to approximate these complex trends observed in the experimental data and capture many of the important features that determine vesicle connectivity in heterogeneous basalts using only sample porosity, approximate extent of microporosity, and assuming random vesicle spatial distributions. Some types of basalt, such as vesicular scoria or other nonrandom vesicle distributions, may require percolation simulations to incorporate vesicle spatial correlations or multipoint statistics. These models advance our ability to approximate and predict the connection between total porosity and effective porosity because it does not rely on regression or empirical techniques but incorporates geologically determined rock geometry, vesicle size and distribution, and microporosity to understand fluid connectivity in vesicular basalt systems.

5. Conclusions and Implications

The relationship between effective porosity and total porosity has important implications for estimating injectivity and storage capacity of carbon dioxide in basalt formations. Both experimental and simulation results from this study indicate that target formations within basalt reservoirs should ideally have total porosities of $\geq$25%, and a minimum total porosity of $\sim$15%, depending on fracturing and microporous behavior, for vesicle connectivity high enough for sustainable injectivity. As with large-scale CO_2 storage reservoirs in sedimentary rocks, the target basalt formation will also need a low permeability seal to retain injected CO_2 until mineral trapping occurs. Several previously published estimates of basalt storage capacity assume complete connectivity in basalts with total porosity values less than 15% (Goldberg et al., 2008; McGrail et al., 2006). Without detailed knowledge of extent and variation in vesicle interconnectivity at low porosity values there is serious potential for overestimating the storage volume in basalt reservoirs. Overestimation of formation capacity and injectivity significantly increases the risk of issues such as induced seismicity (Snæbjörnsdóttir and Gislason, 2016).

Results from simulations also indicate an important trend in surface area of basalts with increasing porosity. As porosity of the material continues to increase above the percolation threshold, both the total and effective surface area begin to decrease due to higher vesicle overlap and connectivity. The trade-off is that ideal carbon storage reservoirs should have maximum porosity and therefore maximum storage volume, however at high porosities there will be less material and mineral surfaces available for geochemical reactions and carbonate mineral formation per volume of rock. This observation is also important in

the context of geothermal energy; higher porosity geothermal reservoirs contain larger volumes of water and steam while higher rock-fluid surface area increases geothermal heat transfer. Site specific studies will be necessary to optimize reservoir performance based on porosity, microporosity, and fracture extent in a given basalt formation.

The methods described in this work will enable better prediction of connectivity and transport in basaltic systems using standard porosity and thin section analysis to determine the percolation model input parameters of porosity and microporous rim dimensions. There is potential for future work to incorporate these percolation models into reactive transport simulations, evaluate the role of fracture density and orientation on system connectivity, and use percolation simulation techniques to better predict permeability and injectivity in basalt reservoirs.

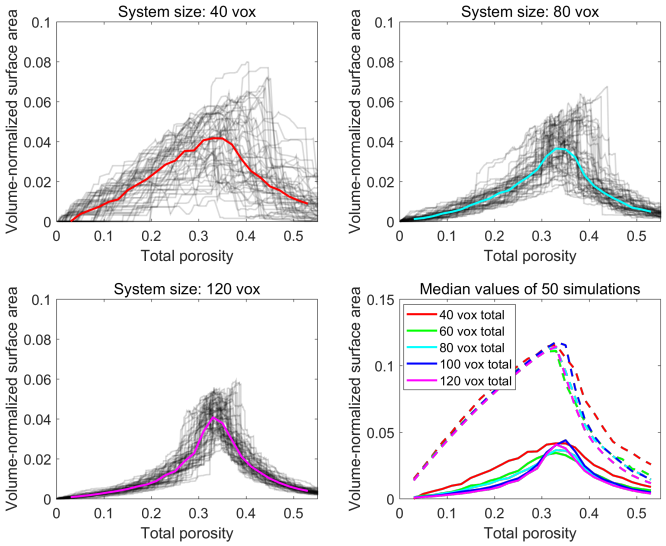

Figure 8: (Upper row and lower left) Comparison of volume-normalized effective surface area for three different systems sizes (e.g. 40 vox means 40 x 40 x 40 grid cell system). Grey lines indicate surface area calculations normalized by system volume. Each line is one simulation run. The solid colored lines show the median values at each porosity increment. (Lower right) Summary of median total (dashed lines) and median effective (solid lines) volume-normalized surface area as a function of total porosity for all five system sizes evaluated.

Acknowledgments

This work is funded by the Global Climate Energy Project, the Stanford Center for Carbon Storage, the France-Stanford Center for Interdisciplinary Studies and the Department of Energy Resources Engineering. The Inveon DPET (micro-PET) scanner was funded by NIH grant number 1S10OD018130-01. Funding for the micro-CT scanner was provided in part by the National Science Foundation (NSF) through the National Nanotechnology Coordinated Infrastructure (NNCI) program under award ECCS-1542152. Nick Vandehey, James O'Neil, Tim Doyle and Frezghi Habte provided essential radioisotope handling training, PET scanner training, instruction, and advice. Eric Oelkers and Siggi Gislason of the CarbFix project provided samples.

Appendix A: Percolation Simulation Sensitivity Analysis

Sensitivity analysis was performed to analyze the effect of total 3D system volume and vesicle size distribution. In order to test the influence of 3D system size, 50 simulations with normal vesicle distributions were performed at five different system sizes, 40, 60, 80, 100, and 120 voxels (i.e. grid cells) per side length. This is equal to 8, 12, 16, 20, and 24 times the mean vesicle radius respectively. Results from this analysis indicate that while the variability between simulation results decreases with increasing system size, the median behavior of 50 simulations in nearly identical as illustrated by the surface area calculations in Figure 8. Due to the low computational cost of the simulations, and to prevent large outlier models, all of the simulations in this study were run at 120 grid cells per side length.

A number of different vesicle size distributions have been observed in literature. Sahagian et al. (1989) recorded normal, lognormal, bimodal, and trimodal vesicle size distributions, while mostly lognormal distributions were observed by Shin et al. (2005); McGrail et al. (2006); Song et al. (2001). Sato et al. (1997) observed unevenly/random distribution of pore sizes in basalt. Based on these observations in literature and the lognormal vesicle radius distributions measured in the experiments, four sets of simulation models were run with random, normal, lognormal, and bimodal vesicle radius distributions (see Figure 9 for example distributions). Results of this vesicle distribution sensitivity analysis indicate that while there is variability from one simulation to another, the median trend of 50 simulations produces nearly identical effective porosity, percolation threshold and effective volume normalized surface area (Figure 10). Results also indicate that vesicle radii distribution does not have a strong influence on the median percolation threshold, which agrees well with observations by Walsh and Saar (2008). There is a slight variation in total volume-normalized surface area because vesicle distributions with large numbers of small vesicles—such as the lognormal distribution—are expected to have a slightly higher surface area to volume ratio, and thus a higher total surface area, at a given total porosity level.

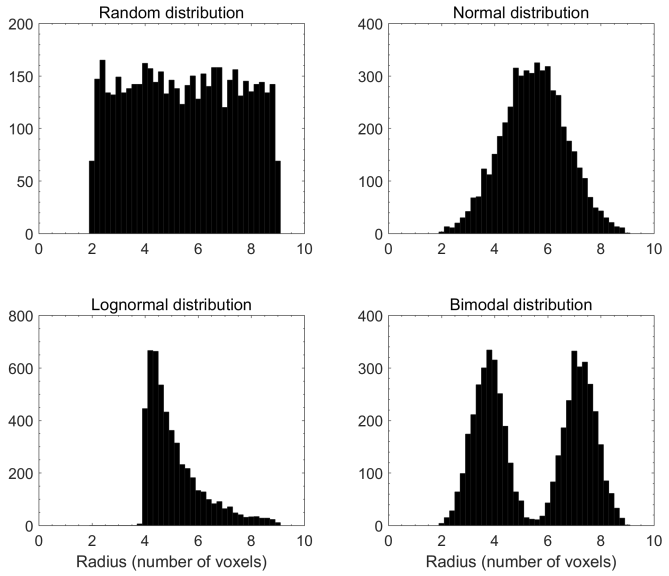

Figure 9: Example vesicle radius distributions used for vesicle size distribution sensitivity analysis. During a simulation run, a large matrix (5000 values) of grid cell radii is created based on desired type of distribution and upper and lower grid cell size limits. For the sensitivity analysis of vesicle size distributions, the mean radius of all of the vesicle size distributions is set to approximately five voxels.

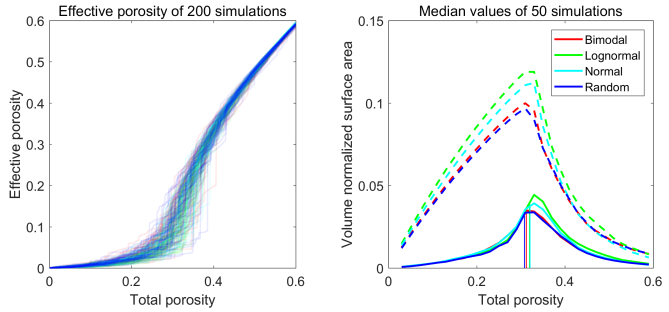

Figure 10: (Left): Effective porosity as a function of total vesical porosity from 200 simulations (50 simulations from each of the four different vesicle distributions). Different line colors indicate different vesicle distributions. (Right) Median effective volume-normalized surface area (solid lines) and total volume normalized surface area (dashed lines) as a function of total vesicle porosity of 50 simulations from each of the four different vesicle distributions. Thin vertical lines indicate the median percolation threshold porosity.

Additional Supplementary Material

- Excel sheet with helium porosity porosity analysis and other experimental data

Bibliography

Alfredsson, H. A., Oelkers, E. H., Hardarsson, B. S., Franzson, H., Gunnlaugsson, E., and Gislason, S. R. (2013). The geology and water chemistry of the Hellisheidi, SW-Iceland carbon storage site. *International Journal of Greenhouse Gas Control*, 12:399–418.

Aradóttir, E. S., Sonnenthal, E. L., Björnsson, G., and Jónsson, H. (2012). Multidimensional reactive transport modeling of CO2 mineral sequestration in basalts at the Hellisheidi geothermal field, Iceland. *International Journal of Greenhouse Gas Control*, 9:24–40.

Bai, L., Baker, D. R., and Hill, R. J. (2010). Permeability of vesicular Stromboli basaltic glass: Lattice Boltzmann simulations and laboratory measurements. *Journal of Geophysical Research*, 115(B7):1–16.

Beckingham, L. E., Mitnick, E. H., Steefel, C. I., Zhang, S., Voltolini, M., Swift, A. M., Yang, L., Cole, D. R., Sheets, J. M., Ajo-Franklin, J. B., DePaolo, D. J., Mito, S., and Xue, Z. (2016). Evaluation of mineral reactive surface area estimates for prediction of reactivity of a multi-mineral sediment. *Geochimica et Cosmochimica Acta*, 188:310–329.

Beckingham, L. E., Steefel, C. I., Swift, A. M., Voltolini, M., Yang, L., Anovitz, L. M., Sheets, J. M., Cole, D. R., Kneafsey, T. J., Mitnick, E. H., Zhang, S., Landrot, G., Ajo-Franklin, J. B., DePaolo, D. J., Mito, S., and Xue, Z. (2017). Evaluation of accessible mineral surface areas for improved prediction of mineral reaction rates in porous media. *Geochimica et Cosmochimica Acta*, 205:31–49.

Benson, S. and Cook, P. (2005). Underground geological storage. *IPCC Speacial Report on Carbon Dioxide Capture and Storage, Chapter 5*.

Blower, J. (2001). A three-dimensional network model of permeability in vesicular material. *Computers & Geosciences*, 27(1):115–119.

Boutchko, R., Rayz, V. L., Vandehey, N. T., O'Neil, J. P., Budinger, T. F., Nico, P. S., Druhan, J. L., Saloner, D. a., Gullberg, G. T., and Moses, W. W. (2012). Imaging and modeling of flow in porous media using clinical nuclear emission tomography systems and computational fluid dynamics. *Journal of Applied Geophysics*, 76:74–81.

Brattekas, B., Steinsbo, M., Graue, A., Ferno, M., Espedal, H., and Seright, R. (2016). New Insight to Wormhole Formation in Polymer Gel During Water Chasefloods using Positron Emission Tomography PET. *SPE 180051*, pages 1–13.

Callow, B., Falcon-Suarez, I., Ahmed, S., and Matter, J. (2018). Assessing the carbon sequestration potential of basalt using X-ray micro-CT and rock mechanics. *International Journal of Greenhouse Gas Control*, 70(August 2017):146–156.

Colombier, M., Wadsworth, F. B., Gurioli, L., Scheu, B., Kueppers, U., Di Muro, A., and Dingwell, D. B. (2017). The evolution of pore connectivity in volcanic rocks. *Earth and Planetary Science Letters*, 462:99–109.

Costa, A. (2006). Permeability-porosity relationship: A reexamination of the Kozeny-Carman equation based on a fractal pore-space geometry assumption. *Geophysical Research Letters*, 33(2):1–5.

Ellis, S. R. and Wright, J. L. (2006). Modeling of aqueous transport in rigid porous matrices near the percolation threshold. *Pharmaceutical Research*, 23(10):2441–2453.

Farquharson, J., Heap, M. J., Varley, N. R., Baud, P., and Reuschlé, T. (2015). Permeability and porosity relationships of edifice-forming andesites: A combined field and laboratory study. *Journal of Volcanology and Geothermal Research*, 297:52–68.

Fernø, M. A., Hauge, L. P., Uno Rognmo, A., Gauteplass, J., and Graue, A. (2015). Flow visualization of CO 2 in tight shale formations at reservoir conditions. *Geophysical Research Letters*, 42(18):7414–7419.

Franzson, H., Zierenberg, R., and Schiffman, P. (2008). Chemical transport in geothermal systems in Iceland. Evidence from hydrothermal alteration. *Journal of Volcanology and Geothermal Research*, 173(3-4):217–229.

Gerke, H. H. and van Genuchten, M. (1993). Dual porosity model for simulating the prefrential movement of water and solutes in structured porous media. *Water Resources Research*, 29(2):305–319.

Gislason, S. R. and Oelkers, E. H. (2014). Carbon storage in basalt. *Science*, 344(6182):373–374.

Goethals, P., Volkaert, A., Jacobs, P., Roels, S., and Carmeliet, J. (2009). Comparison of Positron Emission Tomography and X-ray radiography for studies of physical processes in sandstone. *Engineering Geology*, 103(3-4):134–138.

Goldberg, D. S., Kent, D. V., and Olsen, P. E. (2010). Potential on-shore and off-shore reservoirs for CO2 sequestration in Central Atlantic magmatic province basalts. *Proceedings of the National Academy of Sciences*, 107(4):1327–1332.

Goldberg, D. S., Takahashi, T., and Slagle, A. L. (2008). Carbon dioxide sequestration in deep-sea basalt. *Proceedings of the National Academy of Sciences*, 105(29):9920–9925.

Heap, M. J., Lavallée, Y., Petrakova, L., Baud, P., Reuschlé, T., Varley, N. R., and Dingwell, D. B. (2014). Microstructural controls on the physical and mechanical properties of edifice-forming andesites at Volcán de Colima, Mexico. *Journal of Geophysical Research: Solid Earth*, 119(4):2925–2963.

Holloway, S., Garg, A., Kapshe, M., Deshpande, A., Pracha, A., Khan, S., Mahmood, M., Singh, T., Kirk, K., and Gale, J. (2009). An assessment of the CO2 storage potential of the Indian subcontinent. *Energy Procedia*, 1:2607–2613.

Hu, Y., Armstrong, R. T., Hung, T.-t., Lee, B., Shikhov, I., and Mostaghimi, P. (2017). Analysing Flow in Rocks By Combined Positron Emission Tomography and Computed Tomography Imaging. *Society of Core Analysts*, 082:1–9.

Hudson, H. M. and Larkin, R. S. (1994). Ordered Subsets of Projection Data. *IEEE transactions on medical imaging*, 13(4):601–609.

Iassonov, P., Gebrenegus, T., and Tuller, M. (2009). Segmentation of X-ray computed tomography images of porous materials: A crucial step for characterization and quantitative analysis of pore structures. *Water Resources Research*, 45(9):1–12.

Kulenkampff, J., Gründig, M., Zakhnini, A., Gerasch, R., and Lippmann-Pipke, J. (2015). Process tomography of diffusion, using PET, to evaluate anisotropy and heterogeneity. *Clay Minerals*, 50(3):369–375.

Kumar, A., Shrivastava, J. P., and Pathak, V. (2017). Mineral carbonation reactions under water-saturated, hydrothermal-like conditions and numerical simulations of CO2 sequestration in tholeiitic basalt of the Eastern Deccan Volcanic Province, India. *Applied Geochemistry*, 84:87–104.

Kushnir, A. R., Martel, C., Bourdier, J. L., Heap, M. J., Reuschlé, T., Erdmann, S., Komorowski, J. C., and Cholik, N. (2016). Probing permeability and microstructure: Unravelling the role of a low-permeability dome on the explosivity of Merapi (Indonesia). *Journal of Volcanology and Geothermal Research*, 316:56–71.

Lamur, A., Kendrick, J. E., Eggertsson, G. H., Wall, R. J., Ashworth, J. D., and Lavallée, Y. (2017). The permeability of fractured rocks in pressurised volcanic and geothermal systems. *Scientific Reports*, 7:1–9.

Landrot, G., Ajo-Franklin, J. B., Yang, L., Cabrini, S., and Steefel, C. I. (2012). Measurement of accessible reactive surface area in a sandstone, with application to CO2 mineralization. *Chemical Geology*, 318-319:113–125.

Lippmann-Pipke, J., Gerasch, R., Schikora, J., and Kulenkampff, J. (2017). Benchmarking PET for geoscientific applications: 3D quantitative diffusion coefficient determination in clay rock. *Computers & Geosciences*, 101:21–27.

Luhmann, A. J., Tutolo, B. M., Bagley, B. C., Mildner, D. F. R., Seyfried, W. E., and Saar, M. O. (2017). Permeability, porosity, and mineral surface area changes in basalt cores induced by reactive transport of CO2-rich brine. *Water Resources Research*, 53:1908–1927.

Manning, C. E. and Bird, D. K. (1991). Porosity evolution and fluid flow in the basalts of the Skaergaard magma-hydrothermal system, east Greenland. *American Journal of Science*, 291:201–257.

Matter, J. M., Stute, M., Snæbjörnsdottir, S. O., Oelkers, E. H., Gislason, S. R., Aradottir, E. S., Sigfusson, B., Gunnarsson, I., Alfredsson, H. A., Wolff-boenisch, D., Mesfin, K., Dideriksen, K., and Broecker, W. S. (2016). Rapid carbon mineralization for permanent disposal of anthropogenic carbon dioxide emissions. *Science*, 352(6291):1312–1314.

McGrail, B. P., Schaef, H. T., Ho, A. M., Chien, Y.-J., Dooley, J. J., and Davidson, C. L. (2006). Potential for carbon dioxide sequestration in flood basalts. *Journal of Geophysical Research: Solid Earth*, 111(B12):1–13.

McGrail, B. P., Schaef, H. T., Spane, F. A., Cliff, J. B., Qafoku, O., Horner, J. A., Thompson, C. J., Owen, A. T., and Sullivan, C. E. (2017). Field Validation of Supercritical CO2 Reactivity with Basalts. *Environmental Science & Technology Letters*, 4(1):6–10.

Michael, K., Golab, A., Shulakova, V., Ennis-King, J., Allinson, G., Sharma, S., and Aiken, T. (2010). Geological storage of CO2 in saline aquifersA review of the experience from existing storage operations. *International Journal of Greenhouse Gas Control*, 4:659–667.

Mueller, S., Melnik, O., Spieler, O., Scheu, B., and Dingwell, D. B. (2005). Permeability and degassing of dome lavas undergoing rapid decompression: An experimental determination. *Bulletin of Volcanology*, 67:526–538.

Navarre-Sitchler, A., Steefel, C. I., Yang, L., Tomutsa, L., and Brantley, S. L. (2009). Evolution of porosity and diffusivity associated with chemical weathering of a basalt clast. *Journal of Geophysical Research*, 114(F02016):1–14.

Navarre-Sitchler, A. K., Cole, D. R., Rother, G., Jin, L., Buss, H. L., and Brantley, S. L. (2013). Porosity and surface area evolution during weathering of two igneous rocks. *Geochimica et Cosmochimica Acta*, 109:400–413.

Norton, D. and Knapp, R. (1977). Transport phenomena in hydrothermal systems: The nature of porosity. *American Journal of Science*, 277:913–936.

Perrin, J. C. and Benson, S. (2010). An experimental study on the influence of sub-core scale heterogeneities on CO2 distribution in reservoir rocks. *Transport in Porous Media*, 82(1):93–109.

Pini, R., Vandehey, N. T., Druhan, J., and Neil, J. P. O. (2016). Quantifying solute spreading and mixing in reservoir rocks using 3D PET imaging. *Journal of Fluid Mechanics*, 796:558–587.

Polacci, M., Baker, D. R., Bai, L., and Mancini, L. (2008). Large vesicles record pathways of degassing at basaltic volcanoes. *Bulletin of Volcanology*, 70(9):1023–1029.

Polacci, M., Baker, D. R., La Rue, A., Mancini, L., and Allard, P. (2012). Degassing behaviour of vesiculated basaltic magmas: An example from Ambrym volcano, Vanuatu Arc. *Journal of Volcanology and Geothermal Research*, 233-234:55–64.

Rezvani Khalilabad, M., Axelsson, G., and Gislason, S. R. (2008). Aquifer characterization with tracer test technique; permanent CO2 sequestration into basalt, SW Iceland. *Mineralogical Magazine*, 72(1):121–125.

Saar, M. O. (1998). *The Relationship Between Permeability, Porosity, and Microstructure in Vesicular Basalts*. PhD thesis.

Saar, M. O. and Manga, M. (1999). Permeability-porosity relationship in vesicular basalts. *Geophysical Research Letters*, 26(1):111–114.

Sahagian, D. L., Anderson, A. T., and Ward, B. (1989). Bubble coalescence in basalt flows: comparison of a numerical model with natural examples. *Bulletin of Volcanology*, 52(1):49–56.

Sahimi, M. U. o. S. C. (1994). *Applications of percolation theory*. Taylor & Francis, London.

Sato, H., Shibutani, T., and Yui, M. (1997). Experimental and modelling studies on diffusion of Cs, Ni and Sm in granodiorite, basalt and mudstone. *Journal of Contaminant Hydrology*, 26:119–133.

Scientific, T. F. (2018). Avizo Software 9 User 's Guide. 9:1– 915.

Shin, H., Lindquist, W. B., Sahagian, D. L., and Song, S. R. (2005). Analysis of the vesicular structure of basalts. *Computers and Geosciences*, 31(4):473–487.

Shrivastava, P., Rani, N., and Pathak, V. (2016). Geochemical Modeling and Experimental Studies on Mineral Carbonation of Primary Silicates for Long-term Immobilization of CO2 in Basalt from the Eastern Deccan Volcanic Province. *Journal of Indian Geophysics*, 1:42–58.

Sigurosson, O., Guomundsson, A., Frioleifsson, G., Franzson, H., Guolaugsson, S., and Stefansson, V. (2000). Database on igneous rock properties in icelandic geothermal systems. Status and unexpected results. *Proceedings World Geothermal Congress 2000*, pages 2881–2886.

Snæbjörnsdóttir, S. and Gislason, S. R. (2016). CO2 storage potential of basaltic rocks offshore Iceland. *Energy Procedia*, 86:371–380.

Snæbjörnsdóttir, S., Gislason, S. R., Galeczka, I. M., and Oelkers, E. H. (2018). Reaction path modelling of in-situ mineralisation of CO2at the CarbFix site at Hellisheidi, SW-Iceland. *Geochimica et Cosmochimica Acta*, 220:348–366.

Snæbjörnsdóttir, S., Wiese, F., Fridriksson, T., Ármansson, H., Einarsson, G. M., and Gislason, S. R. (2014). CO2 storage potential of basaltic rocks in Iceland and the oceanic Ridges. *Energy Procedia*, 63:4585–4600.

Socolow, R. and Pacala, S. (2004). Stabilization Wedges: Solving the Climate Problem for the Next Half-Century with Technologies Available Today. *Science*, 305(5686):968–972.

Song, S. R., Jones, K. W., Lindquist, W. B., Dowd, B. A., and Sahagian, D. L. (2001). Synchrotron X-ray computed microtomography: Studies on vesiculated basaltic rocks. *Bulletin of Volcanology*, 63(4):252–263.

Szulczewski, M. L., MacMinn, C. W., Herzog, H. J., and Juanes, R. (2012). Lifetime of carbon capture and storage as a climate-change mitigation technology. *Proceedings of the National Academy of Sciences*, 109(14):5185–5189.

Thomas, D. (2018). *GEOCHEMISTRY OF CO2 SEQUESTRATION IN BASALTS: IMPLICATIONS FROM NATURAL ANALOGUES AND EXPERIMENTAL OBSERVATIONS*. Phd thesis, Stanford University.

Tollefson, J. (2013). Pilot projects bury carbon dioxide in basalt. *Nature*, 500(7460):18.

Vincent, L. and Soille, P. (1991). Watersheds in digital spaces: an efficient algorithm based on immersion simulations. *IEEE Transactions on Pattern Analysis and Machine Intelligence*, 13(6):583–598.

Walsh, S. D. C. and Saar, M. O. (2008). Magma yield stress and permeability: Insights from multiphase percolation theory. *Journal of Volcanology and Geothermal Research*, 177(4):1011–1019.

Washburn, E. W. and Bunting, E. N. (1922). Porosity: Vi. Determination of Porosity By the Method of Gas Expansion. *Journal of the American Ceramic Society*, 5(2):112–130.

Wells, R. K., Xiong, W., Giammar, D., and Skemer, P. (2017). Dissolution and surface roughening of Columbia River flood basalt at geologic carbon sequestration conditions. *Chemical Geology*, 467:100–109.

Wolff-Boenisch, D. and Galeczka, I. M. (2018). Flow-through reactor experiments on basalt-(sea)water-CO2 reactions at 90 C and neutral pH. What happens to the basalt pore space under post-injection conditions? *International Journal of Greenhouse Gas Control*, 68:176–190.

Zahasky, C. and Benson, S. (2018). Micro-positron emission tomography for measuring sub-core scale single and multiphase transport parameters in porous media. *Advances in Water Resources*, 115.